

# Cosmic voids detection without density measurements

Andrii Elyiv<sup>1,2\*</sup>, Federico Marulli<sup>1,3,4</sup>, Giorgia Pollina<sup>1,5</sup>, Marco Baldi<sup>1,3,4</sup>,  
Enzo Branchini<sup>6,7,8</sup>, Andrea Cimatti<sup>1</sup> and Lauro Moscardini<sup>1,3,4</sup>

<sup>1</sup>*Dipartimento di Fisica e Astronomia, Università di Bologna, viale Berti Pichat 6/2, 40127 Bologna, Italy*

<sup>2</sup>*Main Astronomical Observatory, Academy of Sciences of Ukraine, 27 Akademika Zabolotnoho St., 03680 Kyiv, Ukraine*

<sup>3</sup>*INAF - Osservatorio Astronomico di Bologna, via Ranzani 1, 40127 Bologna, Italy*

<sup>4</sup>*INFN - Sezione di Bologna, viale Berti Pichat 6/2, 40127 Bologna, Italy*

<sup>5</sup>*University Observatory Munich, Ludwig-Maximilian University, Scheinerstr. 1, 81679, Munich, Germany*

<sup>6</sup>*Dipartimento di Fisica, Università degli Studi Roma Tre, via della Vasca Navale 84, 00146 Rome, Italy*

<sup>7</sup>*INAF - Osservatorio Astronomico di Roma, Monte Porzio Catone, Italy*

<sup>8</sup>*INFN - Sezione di Roma Tre, via della Vasca Navale 84, 00146 Rome, Italy*

Released 2014 October 15

## ABSTRACT

Cosmic voids are effective cosmological probes to discriminate among competing world models. Their identification is generally based on density or geometry criteria that, because of their very nature, are prone to shot noise. We propose two void finders that are based on dynamical criterion to select voids in Lagrangian coordinates and minimise the impact of sparse sampling. The first approach exploits the Zel’dovich approximation to trace back in time the orbits of galaxies located in voids and their surroundings, the second uses the observed galaxy-galaxy correlation function to relax the objects’ spatial distribution to homogeneity and isotropy. In both cases voids are defined as regions of the negative velocity divergence, that can be regarded as sinks of the back-in-time streamlines of the mass tracers. To assess the performance of our methods we used a dark matter halo mock catalogue CoDECS, and compared the results with those obtained with the ZOBOV void finder. We find that the void divergence profiles are less scattered than the density ones and, therefore, their stacking constitutes a more accurate cosmological probe. The significance of the divergence signal in the central part of voids obtained from both our finders is 60% higher than for overdensity profiles in the ZOBOV case. The ellipticity of the stacked void measured in the divergence field is closer to unity, as expected, than what is found when using halo positions. Therefore our void finders are complementary to the existing methods, that should contribute to improve the accuracy of void-based cosmological tests.

**Key words:** methods: data analysis – large-scale structure of Universe

## 1 INTRODUCTION

Cosmic voids are regions of low density that occupy a significant fraction of the volume in the Universe. The first observational evidence of giant voids was obtained more than 30 years ago (Joeveer et al. 1978; Gregory & Thompson 1978). However, their systematic and quantitative study came later with the advent of the first large spectroscopic surveys (Huchra et al. 1988; Geller & Huchra 1989; Bahcall 1995). Now it is well established that void sizes span a wide range of scales, from minivoids with diameters of about 3–5 Mpc in the Local Universe (Tikhonov & Karachentsev 2006) to the supervoids with diameters of about 200 Mpc (Lindner et al.

1995; Szapudi et al. 2014). Due to large volume filling factor, characteristic shape, dynamics and low density, they constitute unique laboratories for astrophysics and cosmology.

In the framework of high energy astrophysics, voids can be regarded as *highways* for propagating particles like cosmic rays and neutrinos (Schlickeiser et al. 2012; Miniati & Elyiv 2013; Krakau & Schlickeiser 2014), in which the presence of non-zero extragalactic magnetic fields or extragalactic light is still an open issue (Elyiv et al. 2009; DeLavallaz & Fairbairn 2012; Beck et al. 2013; Arlen & Vassiliev 2013). Voids are also important for testing galaxy evolution models since they allow to study the evolution of isolated objects and assess, by comparison, the influence of the environment (Peebles 2001; Patiri et al. 2006; Vavilova et al. 2009; Stanonik et al. 2010; Nicholls et al. 2014). Indeed, the deficit of dwarf galax-

\* E-mail: andrii.elyiv@unibo.it

ies in nearby voids (Peebles 2001; Kreckel et al. 2011; Elyiv et al. 2013) with respect to the theoretical prediction, often dubbed as the *Void Phenomenon*, is still regarded as a potential evidence against the cold dark matter (CDM) scenario.

Finally, and most importantly, voids are very relevant for cosmology. They have an impact on the Cosmic Microwave Background and on the weak lensing signal. Anomalies like the Cold Spot could be explained as the result of the Integrated Sachs-Wolfe effect over large voids (Rees & Sciama 1968; Szapudi et al. 2014; Kovács et al. 2014). Next generation galaxy surveys like those that will be carried out by the Large Synoptic Survey Telescope (Kaiser et al. 2002) and by the Euclid satellite (Laureijs et al. 2011; Amendola et al. 2013) are expected to detect gravitational lensing from medium-sized voids with which one can constrain the void's mass density profile without using galaxies and assumptions on their bias (Izumi et al. 2013; Krause et al. 2013; Melchior et al. 2014; Clampitt & Jain 2014).

Indeed, voids can be used as effective cosmological probes. Their physical properties depend on the nature of dark energy (DE) and on the primordial density field from which they have evolved (Odrzywolek 2009; D'Amico et al. 2011; Bos et al. 2012; Spolyar et al. 2013; Gibbons et al. 2014). In particular, it has been realised that their shape is very sensitive to the equation of state of the DE component and that spurious ellipticity could be used to constrain the amount of dark matter (DM) (Lavaux & Wandelt 2010). Additional constraints on DM can also be obtained by measuring the outflow velocities from voids in the nearby Universe (Courtois et al. 2012; Tully et al. 2013). Finally, voids' expansion history and shape have been used to test modified gravity models (Li 2011; Clampitt et al. 2013; Zivick & Sutter 2014; Cai et al. 2014).

Perhaps their most common and effective cosmological application is through the so-called Alcock-Paczynski (AP) test (Alcock & Paczynski 1979), in which one measures the size of the stacked void along and across the line of sight and looks for a possible mismatch that would arise from assuming an incorrect cosmological model (Sutter et al. 2012, 2014). The accuracy of the AP test has been discussed in comparison to that of other cosmological tests by Lavaux & Wandelt (2012). The first application of the method by Sutter et al. (2012) considered voids extracted from the SDSS DR-7 galaxy survey (Abazajian et al. 2009) using a modified version of the ZOnes Bordering On Voidness (ZOBOV) algorithm (Neyrinck 2008). With 10 stacked voids detected out to  $z = 0.36$  they failed to detect any significant distortions. In a more recent attempt by Sutter et al. (2014) that used the SDSS-DR10 LOWZ and CMASS galaxy samples (Ahn et al. 2014), the AP signal corresponding to a mass density parameter  $\Omega_M \approx 0.15$  has been detected.

The accuracy of the AP test depends on the ability to identify voids in a reliable and robust way. This is not an easy task, as demonstrated by the fact that many different void finders have been proposed over the years, many of which cross-compared in the Aspen-Amsterdam contest (Colberg et al. 2008). Lavaux & Wandelt (2010) proposed to classify void finders in three different categories depending on the type of criterion adopted for the identification. The first class is based on a density criterion and defines voids as regions empty of galaxies or with local density well below the mean (Gottlöber et al. 2003; Colberg et al. 2005; Brunino et al. 2007; Elyiv et al. 2013). The second class uses geometry criteria and identifies voids as geometrical structures like e.g. spherical cells, polyhedra, etc. (Plionis & Basilakos 2002; Colberg et al. 2005; Shandarin et al. 2006; Platen et al. 2007; Neyrinck 2008; Leclercq et al. 2014). The third class is that of finders based on dynamical criteria in which galaxies are considered as test particles of the

cosmic velocity field and not as tracers of the underlying mass distribution (Hahn et al. 2007; Lavaux & Wandelt 2010).

Finders of the first two classes identify voids from galaxies' Eulerian positions. This strategy has two disadvantages. First of all, galaxies are used as mass tracers and some biasing prescription has to be adopted to specify the relation between the galaxy and the mass density field. This might play a significant role when attempting to use cosmic voids to distinguish different cosmological scenarios, in particular different theories of gravity or couplings in the dark sector, as these models might feature a non-standard evolution of the halo bias (Pollina et al. 2014). Second, voids are by definition low density regions. Any method that uses galaxies to identify voids is then prone to shot noise error. Nadathur et al. (2014) showed that the naive strategy of measuring density in spherical shells around voids leads to a large number of empty shells and, consequently, a systematic underestimate of the density profile. An additional drawback related to the Eulerian nature of these methods is that they identify structures in a broad range of dynamical regimes, which complicates the comparison with theoretical predictions.

An advantage of void finders of the third class is that they can be defined in Lagrangian coordinates, which greatly alleviates the shot noise problem and eases the theoretical interpretation of the results. The disadvantage, however, is that voids selected cannot be readily compared with those obtained with the other methods. Perhaps, the best worked out example of dynamical Lagrangian void finder is the DIVA method proposed by Lavaux & Wandelt (2010). This technique uses the Monge-Ampère-Kantorovitch method (Brenier et al. 2003) to reconstruct galaxy orbits back in time starting from their Eulerian position, and identifies voids in Lagrangian coordinates by looking at the regions where the divergence of the displacement field is positive. Assuming approximate correspondence between the divergence field and linearly extrapolated initial density field, they made predictions on void statistics and local ellipticities defined from the curvature of the divergence field. Dynamical void finders from the last class are very promising for the probe of precision cosmology.

In this work we propose two dynamical void finders of the third class. Both methods aim at reconstructing galaxies' Lagrangian positions by randomising the Eulerian ones. The randomisation, however, is achieved in two different ways. The first exploits galaxy clustering, and more specifically the observed two-point correlation function, and relaxes the system to a homogeneous and isotropic distribution using, in reverse, an annealing scheme similar to the one proposed by Rintoul & Torquato (1997) and commonly used in solid state physics to create samples with specified spatial correlation properties. The second method is not completely new and actually quite similar to the DIVA method, except that it uses the Path Interchange Zel'dovich Approximation (PIZA) (Croft & Gaztanaga 1997) to reconstruct galaxy orbits that, in this case, are simply straight lines. In this respect, more accurate reconstruction schemes could be used, like those that minimise the action of a non-linear system (Peebles 1989; Nusser & Branchini 2000). However, we decided to adopt the PIZA scheme since it is fast, and easy to implement.

The randomisation procedure allows to build a displacement field which approximates the cosmic velocity field and enables to trace the buildup of cosmic structures, including voids. The latter are defined as sinks in the time reverse streamline of galaxies. This is the criterion that we use to locate voids in the Lagrangian coordinates. We test our void finders using the catalogue of DM haloes extracted from a high-resolution N-body simulation (Baldi 2012)

at  $z = 0$ , and compare our results with those obtained when we use the ZOBOV void finder (Neyrinck 2008). The quantitative comparison focuses on voids' statistics, as well as on physical properties such as their mass density profile and ellipticities.

The paper is organised as follows. In §2 we describe the halo catalogues used in this work. In §3 we present the two proposed void finders based on the two-point correlation function (§3.1) and on the Lagrangian Zel'dovich approximation (§3.2). The procedure used for the final void identification is described in §4. In §5 we analyse the properties of the voids selected with the two methods, and compare them with the ones detected by the ZOBOV finder. The conclusions are drawn in §6.

## 2 THE DM HALO CATALOGUE

In order to test our void finder algorithms, and to compare them with those obtained with the public code ZOBOV, we use a halo catalogue extracted from the CoDECS simulations (Baldi 2012), that are the largest suite of publicly available<sup>1</sup> cosmological and hydrodynamical simulations of interacting Dark Energy cosmologies (Wetterich 1995; Amendola 2000) to date. The CoDECS runs include five different models of DE interaction, plus a reference  $\Lambda$ CDM run.

In this work we focus on the standard  $\Lambda$ CDM run and plan to explore the other interacting Dark Energy models included in the CoDECS Project in a future work aimed at assessing the impact of the dark sector interactions on voids' properties (Pollina et al. 2014). Specifically, we have considered the H-CoDECS run, a hydrodynamical N-body simulation with a comoving box size of 80 Mpc/h and a total number of particles (gas + CDM) of  $N_p = 2 \times 512^3 \approx 2.7 \times 10^8$ . The CDM mass resolution is  $m_c = 2.39 \times 10^8 M_\odot/h$ , and the gravitational softening was set to  $\epsilon_g = 3.5$  kpc/h, corresponding to about 1/40th of the mean inter-particle separation,  $\bar{d}$ . CDM haloes have been identified by means of a Friends-of-Friends (FoF) algorithm (Davis et al. 1985) with linking length  $\lambda = 0.2 \times \bar{d}$ . This procedure has been applied to the particle distribution by linking the CDM particles as primary tracers of the local mass density, and then attaching baryonic particles to the FoF group of their nearest neighbour. The CoDECS public repository provides also spherical overdensity catalogs computed with the SubFind algorithm (Springel et al. 2001), but for the present analysis we will consider only the FoF catalogs. In this work we focus on the  $z = 0$  output. At this epoch the halo catalogue consists of 116129 haloes with a minimum mass of  $7.657 \times 10^{10} M_\odot/h$ , corresponding to an average halo density of  $\rho_h = 0.23$  (Mpc/h)<sup>-3</sup> and to a corresponding mean inter-halo separation of 1.64 Mpc/h. The average halo density is high enough to identify small voids with sizes above 3 Mpc/h, while the large volume of the sample,  $5.12 \times 10^5 \text{ Mpc}^3/h^3$ , may provide a wide range of void sizes up to  $\sim 20$  Mpc/h.

## 3 DYNAMICAL VOID FINDERS

The basic idea behind the two dynamical void finders that we present in this Section is rather simple. Let us consider a volume of the Universe characterised by large scale structures in the DM component and probed by “particles” like haloes or galaxies. Here we propose to use these as test particles, not mass tracers, and trace

their orbits back in time to a homogeneous and isotropic initial distribution, that is to reconstruct their Lagrangian positions  $\mathbf{q}$ . This is done in two ways: *i*) by exploiting the different correlation properties of the initial and final particle distributions and *ii*) by assuming some dynamical approximation that allows to solve the mixed boundary problem of a system of particles with known final positions and well defined initial statistical properties. The practical implementation of these ideas are described in §3.1 and §3.2, respectively.

After reconstructing Lagrangian positions,  $\mathbf{q}$ , we obtain the particle displacement field,  $\Psi$ , by simply connecting them to the Eulerian positions,  $\mathbf{v}$ , hence assuming straight orbits:  $\mathbf{q} - \mathbf{v} = \Psi(\mathbf{q})$ . The divergence of the displacement field,  $\Theta \equiv \nabla \cdot \Psi$ , is associated to the mass density field and used to identify voids as sinks of mass streamlines in time reverse variables. We note that this approach is similar to that of Ricciardelli et al. (2013), in which a positive divergence in the galaxy flow was one of the conditions used to identify voids.

### 3.1 The Uncorrelating Void Finder

At the present epoch the spatial distribution of galaxies is highly inhomogeneous. Deviations from the homogeneity are conveniently and readily characterised by their spatial two-point correlation function that measures the departure from a purely Poisson distribution. On the other hand, at early epochs the distribution of matter and of any test particles like galaxies is supposed to be highly homogeneous, with no spatial correlation. This suggests that a practical way to trace galaxy orbits back in time, at least in a statistical sense, could be that of relaxing their present spatial distribution to homogeneity, practically defined as a state in which the correlation function at all separations is zero. An effective way to achieve this is by applying the annealing method of Rintoul & Torquato (1997) in reverse, effectively moving the system away from its minimum energy configuration. We note that this method has been used to generate mock galaxy catalogues with a specified two-point correlation function (Soares-Santos et al. 2011). In our iterative algorithm we allow for a small random displacement of one halo along a random direction with the length 0.5 Mpc/h. If the amplitude of the two-point correlation function decreases then we place the halo at the new position. Otherwise we keep it at the original position. Then we move to the next halo and repeat the procedure for all haloes in the catalogue. Then we move to the next iteration and start again with the first halo. Iterations stop when the amplitude of the two-point correlation function is consistent with zero within the uncertainties at all separations. More quantitatively, iterations stop when  $\sum_{i=1}^N \xi(r_i)^2 / N_b < \epsilon_{lim}$ , where  $\xi(r_i)$  is the amplitude of the two-point correlation function at separation  $r_i$ , and  $N_b$  is the total number of bins. In this work we used  $N = 50$  logarithmic bins over the range of scales  $0.5 < r[\text{Mpc}/h] < 50$ . We set the tolerance parameter empirically to the value  $\epsilon_{lim} = 10^{-6}$ , as a compromise between reconstruction accuracy and computational cost. For a fast measurement of the two-point correlation function, we use a linked-list based algorithm (Marulli et al. 2012, 2013), specifically modified to update at each iteration step only the number of pairs associated to the halo that is moved in the procedure<sup>2</sup>.

At the various steps of the iteration the haloes describe a random walk from high density regions to low density ones. We com-

<sup>1</sup> See [www.marcobaldi.it/CoDECS](http://www.marcobaldi.it/CoDECS)

<sup>2</sup> Using  $\sim 116000$  haloes as test particles, the code requires  $\sim 100$  hours of CPU time to detect the voids, with an Intel Core i5, 520M@2.4 GHz CPU.

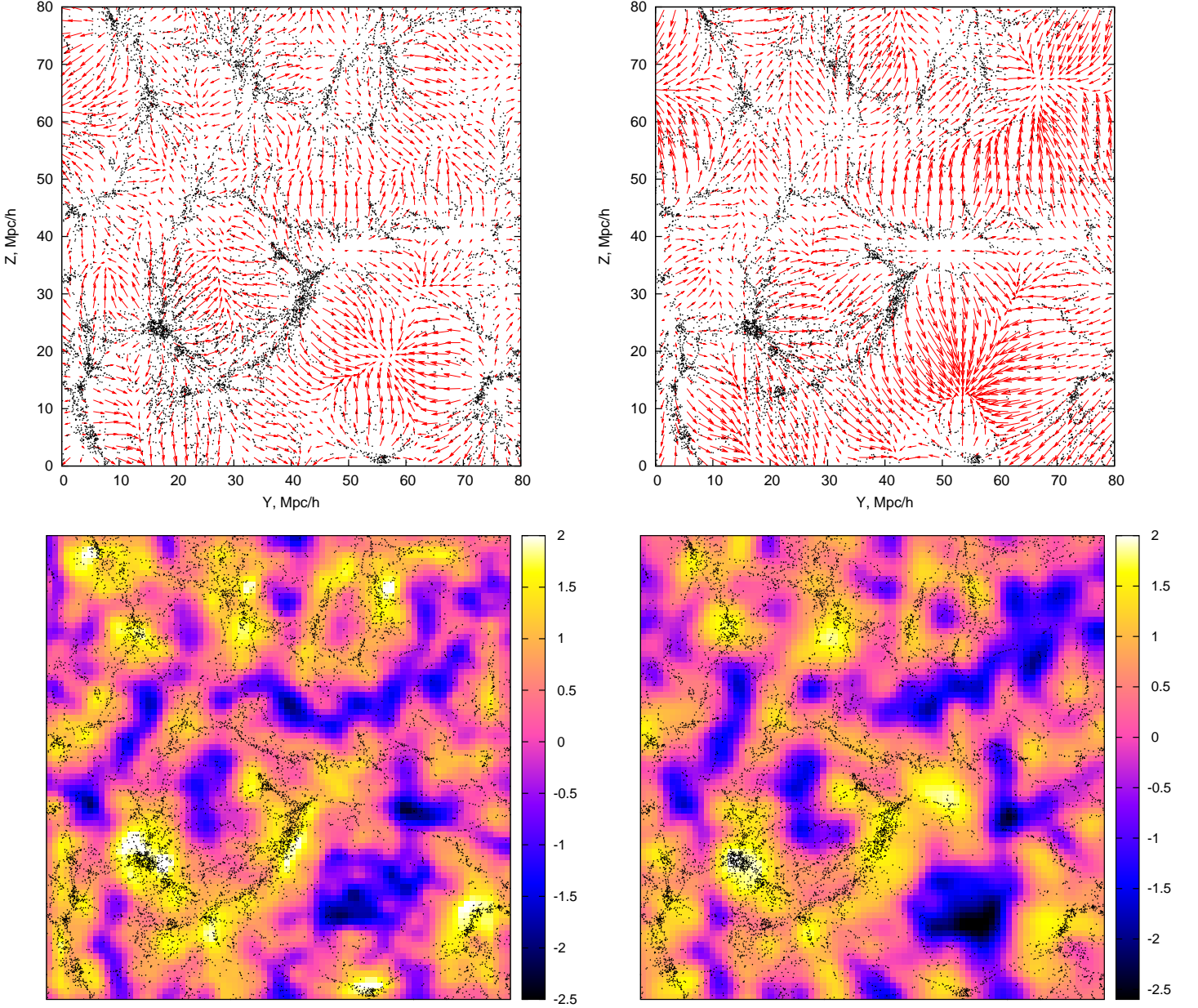


**Figure 1.** The reconstructed displacement field  $\Psi$  (top panels) and its divergence  $\Theta$  (bottom panels), obtained with the two void finders proposed in this work, the UVF (left-hand panels) and the LZVF (right-hand panels). The size of the displayed region is  $80 \times 80$  Mpc/h, with a thickness of 5 Mpc/h. Black dots represent dark matter haloes. The amplitude of the vector field components (red arrows) is reduced by a factor of 0.75, for visual clarity.

pute the displacement vector  $\Psi$  that connects the Eulerian and the reconstructed Lagrangian positions at the end of the iteration. Since the reconstruction is not unique, the Lagrangian positions, and consequently the displacement field, depend on the random seed. We perform 10 reconstructions using different seeds and obtain the average displacement field at the given position  $\mathbf{q}$  by Gaussian-weighting the individual displacement vectors at the different reconstructed Lagrangian positions, that is

$$\langle \Psi(\mathbf{q}) \rangle = \sum_j \Psi_j \cdot \exp(-d_j^2/2\sigma^2) / \sum_j \exp(-d_j^2/2\sigma^2). \quad (1)$$

Here the subscript  $j$  identifies the reconstructed Lagrangian positions in any of the 10 reconstructions and the sum runs over all haloes' Lagrangian positions in the 10 reconstructions,  $d_j$  is the

distance of the halo  $j$  to the given position  $\mathbf{q}$ . Such a Gaussian smoothing is a needed procedure to convert discrete displacement vectors which are computed at the Lagrangian positions of galaxies to a contiguous vector field. The most direct way is Gaussian smoothing with kernel scale  $\sigma = 1.5$  Mpc/h, that corresponds to the mean inter-halo distance. Finally, the displacement field is used to build the divergence field  $\Theta = \nabla \cdot \Psi$  at the generic position  $(x, y, z)$  which, for convenience, we place at the nodes of a cubic grid of size 1 Mpc/h. We shall call this method the *Uncorrelating Void Finder* (UVF).

Fig. 1 shows a slice of thickness 5 Mpc/h across the computational cube. The top left panel shows the Eulerian positions of the haloes (black dots) superimposed to the projected displacement

field ( $\Psi$ ) (red arrows). In the bottom panel the same black dots are superimposed to the divergence field. The colour code is set according to the amplitude of  $\Theta$ , as indicated by the colour bar.

### 3.2 The Lagrangian Zel'dovich Void Finder

The second void finder that we consider here is based on the Zel'dovich approximation (Zel'dovich 1970) to the growth of density fluctuations. More specifically, we implement the PIZA method of Croft & Gaztanaga (1997) to trace the orbit of the objects in a self gravitating system by minimising its action, under the Zel'dovich approximation. Since objects have straight orbits, we simply connect their Eulerian positions to those of a randomly distributed sample. In each iteration we modify the connection, hence setting a new path to a different grid point, and accept it if the total path, obtained by summing the square of the individual paths, decreases. Since the total path is proportional to the action, this system is relaxed to the correct dynamical configuration. We will refer to this finder as the *Lagrangian Zel'dovich Void Finder* (LZVF).

Again, the reconstructed positions depend on the choice of the random seed used in the iterative procedure. The displacement fields obtained from 10 different reconstructions were smoothed by a Gaussian kernel of radius 1.5 Mpc/h, i.e. the same one used in the UVF finder.

The result is shown in the right panels of Fig. 1, that are analogous to their counterpart on the left. Clearly both the divergence and the displacement fields obtained with the two methods are qualitative similar. The main features (coherent flows, regions of large positive/negative divergence) are seen on both reconstructions. However, their amplitude and spatial location do not always coincide. We shall see in the next Sections what are the impacts of these differences on the properties of the voids.

## 4 VOID IDENTIFICATION AND CHARACTERISATION

By definition the divergence of the vector field represents the density,  $\Theta$ , of sources or sinks of that field at a given point:

$$\Theta = \nabla \cdot \Psi = \sum_{i=1}^3 \frac{\partial \Psi_i}{\partial x_i}, \quad (2)$$

where  $x_i$  are the Cartesian coordinates. We calculate the divergence numerically in a grid with step 1 Mpc/h. The colour maps in the lower panels of Fig. 1 show the divergence field assessed with the two proposed void finders, UVF (left) and LZVF (right). Clearly, there is a strong correlation between the distribution of the Eulerian halo positions and the magnitude of divergence calculated in Lagrangian coordinates.

We use the dimensionless quantity  $\Theta$  to characterise the voids, instead of the local density. Specifically, the local minima of the divergence field are used to localize the voids. In our approach, a local minimum is a grid node where  $\Theta$  is lower than in all the adjacent  $3^3 - 1$  nodes around it. Moreover, we consider only the local minima with negative divergence. Each local minimum identifies a subvoid. To determine its shape we use the well known watershed technique (Platen et al. 2007). We fill the basin starting from the local minimum. When the “water” level of a subvoid reaches the ones of adjacent subvoids, we do not join these regions but just put a wall between them and continue by filling until all grid nodes with  $\Theta < 0$  are not involved. In such a way the divergence field divides the space between subvoids around each local minimum. We do not

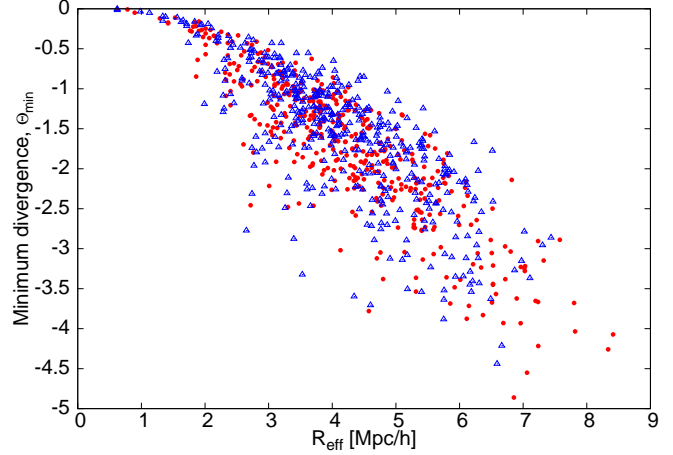


**Figure 2.** Relation between the effective subvoid radii,  $R_{eff}$ , and the divergence minima,  $\Theta_{min}$ , for the two void finders, UVF (blue triangles) and LZVF (red circles).

use any other additional parameters or criteria for the void identification, as the average or minimum halo density. This approach provides a strict definition of subvoids, which can be considered as the sinks of the back-in-time streamlines of the mass tracers. The subvoids are the roots in the tree hierarchy, and have no parent voids. We do not consider subvoids that lie close to the boundary of the sample, as their volumes would be underestimated.

To assess the subvoid as well as void sizes, we estimate the spherical equivalent radius  $R_{eff} = \left(\frac{3V_{void}}{4\pi}\right)^{1/3}$ , where  $V_{void}$  is the volume of the void. We find a moderate correlation between the values of minimum divergence,  $\Theta_{min}$ , and the effective radii of the corresponding subvoids, as shown in Fig. 2. This is expected: the smaller is the minimum divergence, the larger is the subvoid volume around. It can be interpreted according to the large scale structure growing scenario. The larger is a galaxy escaping velocity at a given place, the more effective is the void expanding there, as confirmed theoretically for isolated perturbations of the density field (Bardeen et al. 1986; Sheth & van de Weygaert 2004). This result is in agreement with the findings by Nadathur et al. (2014), obtained using the ZOBOV watershed transform algorithm.

The construction of the void hierarchical tree is not unique. Here we have adopted a procedure based on merging adjacent voids and set the minimum effective radius of accepted voids,  $R_{lim}$ . Voids are said to be adjacent when they have been assigned two nearby grid points. The procedure is the following:

- Voids are sorted by their effective radius from the largest to the smallest.
- Voids with an effective radius larger than  $R_{lim}$  are kept.
- Voids with radius below  $R_{lim}$  that are isolated (that is with no adjacent void) are discarded.
- Voids with radius below  $R_{lim}$  with one or more adjacent voids, are merged to the adjacent one with the largest radius. The effective radius of the new merged void is calculated from the sum of the void volumes that are included in the merged void. We repeat this procedure until all adjacent voids have radii below  $R_{lim}$ .
- After the merging procedure we keep all objects with radius larger than  $R_{lim}$ .

A crucial issue to be addressed when reconstructing void profiles and stacking is how to define the void centres. We consider

four alternative definitions. The first one is the geometrical centre defined as follows:

$$\mathbf{r}_G = \frac{\sum_{i=1}^n \mathbf{r}_i}{n}, \quad (3)$$

where  $\mathbf{r}_i$  are the coordinates of all  $n$  grid nodes that belong to the void, that is  $\mathbf{r}_G$  is the centre of mass if the void density is uniform.

The second definition is the barycentre of the haloes hosted in the void:

$$\mathbf{r}_B = \frac{\sum_{j=1}^N \mathbf{v}_j}{N}, \quad (4)$$

where  $\mathbf{v}_j$  are the coordinates of the  $N$  haloes in the void.

The third void centre is defined as the weighted centre over the divergence field inside a given void:

$$\mathbf{r}_W = \frac{\sum_{i=1}^n \Theta(\mathbf{r}_i) \mathbf{r}_i}{\sum_{i=1}^n \Theta(\mathbf{r}_i)}, \quad (5)$$

where  $\mathbf{r}_i$  are the coordinates of all  $n$  grid nodes that belong to the void.

The last definition considered in this work is the position of the minimum of the divergence field inside a given void,  $\mathbf{r}_M$ . In the following figures, we will refer to these four different definitions of void centres as **G**, **B**, **W**, **M**, respectively.

## 5 RESULTS

Applying our two finders, UVF (§3.1) and LZVF (§3.2), to the  $z = 0$  DM halo sample described in §2, we construct a set of void catalogues. In the following Sections we present the main properties of the selected voids, and compare them to the ones detected by the ZOBOV finder in §5.5.

### 5.1 Void statistics

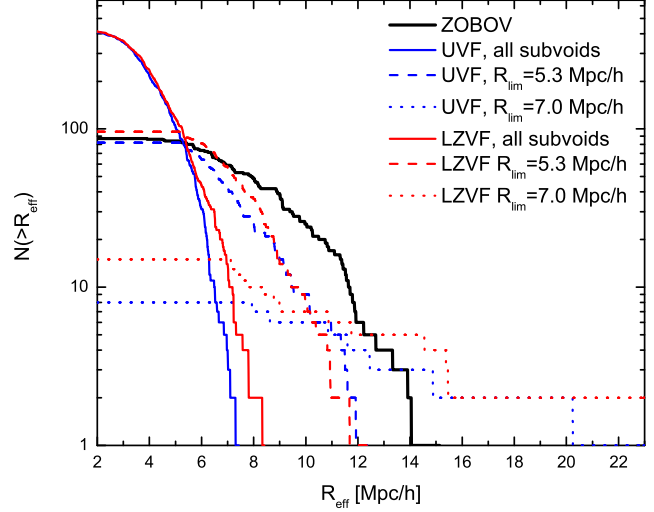
Using the two void finders, UVF and LZVF, we find in total 427 and 433 subvoids, respectively, with effective radii up to  $\sim 8.4 \text{ Mpc}/h$ . We construct different void samples by cutting at different  $R_{lim}$ . The main properties of the selected void catalogues are summarized in Table 1.

Fig. 3 compares the cumulative distributions of voids selected with different finders, as a function of the effective radius  $R_{eff}$ , and for three different values of  $R_{lim}$ . As expected, these distributions become steeper as  $R_{lim}$  decreases. The results obtained with the two finders UVF and LZVF appear in reasonable agreement.

The use of a grid and of a smoothing of the displacement field could in principle introduce a numerical bias in our results. We investigate the impact of these issues by changing the grid steps and the smoothing scale. An increasing of the grid step from 1 to 2 Mpc has the effect of enhancing the median subvoid radii by  $\sim 10\%$ , while the size of the larger merged voids and the divergence profiles are almost unaffected. When increasing the smoothing scale from 1.5 to 3 Mpc/h, the median radii of subvoids are enhanced by  $\sim 30(70)\%$  for  $R_{lim} = 4(0) \text{ Mpc}/h$ , while the sizes of larger voids are unchanged.

### 5.2 Divergence profiles

Fig. 4 shows the mean divergence profiles (*left panel*) and associated  $1\sigma$  deviations (*right panel*) as a function of the normalized distance  $d/R_{eff}$  from the void centres. In particular, this figure shows



**Figure 3.** The cumulative distribution of selected voids as a function of  $R_{eff}$ , for different values of  $R_{lim}$ , as indicated by the labels. Blue, red and black lines show the results obtained with UVF, LZVF and ZOBOV, respectively.

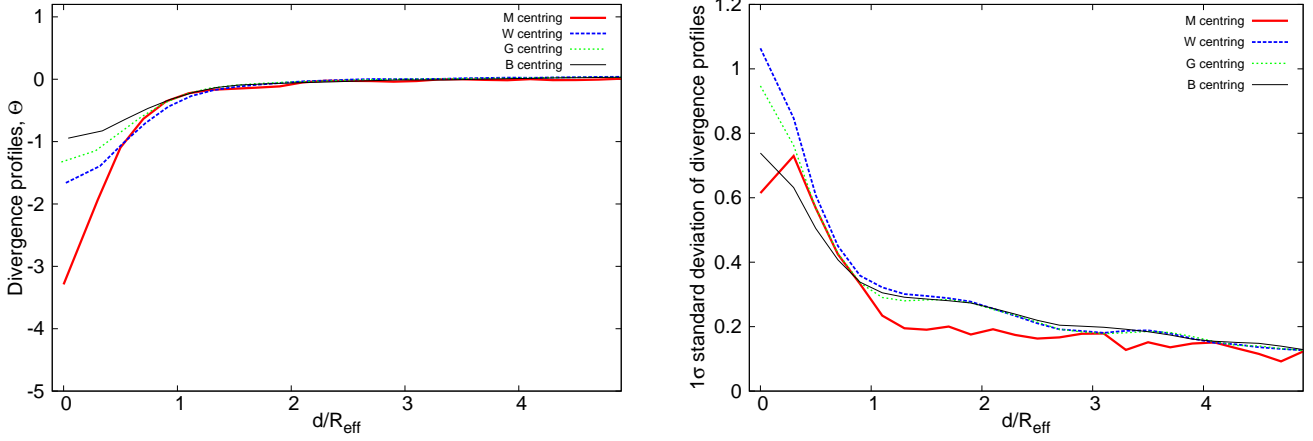
**Table 1.** Main properties of the void samples selected with UVF, LZVF (for different values of  $R_{lim}$ ) and ZOBOV.

void sample, $R_{lim}$ [Mpc/h]	number of voids	$R_{eff}$ range [Mpc/h]	median $R_{eff}$ [Mpc/h]
UVF finder			
all subvoids	427	0.6 - 7.4	4.0
2	405	2.0 - 7.4	4.1
3	344	3.0 - 7.4	4.4
4	211	4.0 - 8.0	5.4
5	103	5.0 - 11.6	6.8
5.3	82	5.3 - 12.6	7.0
6	34	6.0 - 17.1	8.3
7	8	7.0 - 28.7	12.0
8	7	8.0 - 28.7	12.5
LZVF finder			
all subvoids	433	0.6-8.4	4.1
2	412	2.0-8.4	4.2
3	358	3.0-8.5	4.4
4	233	4.0-8.5	5.3
5	117	5.0-12.2	6.9
5.3	96	5.3-12.6	7.3
6	46	6.0-17.9	8.5
7	15	7.0-26.5	9.0
8	5	8.0 - 32.2	17.5
ZOBOV	87	3.9 - 15.1	8.2

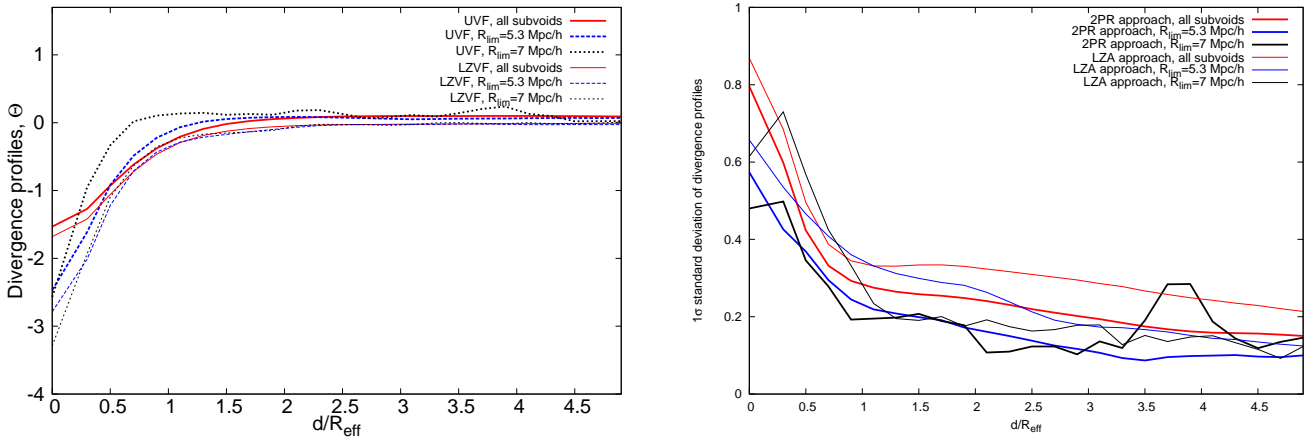
the impact of the different definitions of void centres considered in this work. As it can be seen in the left panel, the divergence profiles obtained with the **M** centring, that is by defining the void centres as the minima of the divergence field, are the steepest in the central part and the least noisy. Therefore, in the following analysis we will consider only this definition.

Fig. 5 compares the results obtained with UVF and LZVF, for





**Figure 4.** Mean divergence profiles (*left-hand panel*) and corresponding  $1\sigma$  deviations (*right-hand panel*) of the voids detected by the LZVF, as a function of the normalized radial distance,  $d/R_{\text{eff}}$ , and for different centring, as indicated by the labels.



**Figure 5.** Mean divergence profiles (*left-hand panel*) and corresponding  $1\sigma$  deviations (*right-hand panel*) of the voids detected by the two finders UVF and LZVF, as a function of the normalized radial distance,  $d/R_{\text{eff}}$ , and for three different values of  $R_{\text{lim}}$  (**M** centring), as indicated by the labels.

three different values of  $R_{\text{lim}} = 0, 5.3$  and  $7 \text{ Mpc/h}$  (with **M** centring). While the mean divergence profiles of the two void finders are in close agreement, we note that the ones provided by UVF are the least noisy, independent of  $R_{\text{lim}}$ . As the selected voids are not exactly spherical, the outer parts of these profiles can include also regions outside the voids. The effect is however low, and does not significantly impact our results.

### 5.3 Overdensity profiles

Fig. 6 compares the mean overdensity profiles and corresponding  $1\sigma$  deviations of the subvoids, moderate ( $R_{\text{lim}} = 5.3 \text{ Mpc/h}$ ) and large voids ( $R_{\text{lim}} = 7 \text{ Mpc/h}$ ) detected by our two finders, assuming the **M** centring. The profiles appear quite smooth, flattening at around  $2R_{\text{eff}}$ . Most of them are not compensated, differently from what is obtained using void finders based on density measurements (see §5.5). We find also very few voids with positive overdensity in the central radial bin, due to the cloud-in-void mode of the void hierarchy (Sheth & van de Weygaert 2004). The  $1\sigma$  deviations of the overdensity profiles decrease for larger values of  $R_{\text{lim}}$ , especially at small radial distances. Overall, the mean void profiles obtained with the two finders UVF and LZVF appear in good agreement.

Divergence, overdensity and shape parameters of the selected void samples are reported in Table 2.

### 5.4 Void ellipticities

To further investigate the characteristics of the selected samples, we estimate the ellipticity of stacked voids. We consider three sub-samples: subvoids with  $4 < r_{\text{eff}} [\text{Mpc/h}] < 7$ , moderate voids with  $7 < r_{\text{eff}} [\text{Mpc/h}] < 10$  and  $R_{\text{lim}} = 5.3 \text{ Mpc/h}$ , and large voids with  $r_{\text{eff}} > 7 \text{ Mpc/h}$  and  $R_{\text{lim}} = 7 \text{ Mpc/h}$ . To measure the ellipticity in the divergence field, we use the second moments of the  $\Theta$  distribution at the void position. The components of the inertial tensor are defined in Lagrangian space with respect to the void centres:

$$I_{i,j} = \sum \chi_i \chi_j \Theta(\mathbf{q}), \quad (6)$$

where the smoothed divergence field  $\Theta$  is defined over the nodes of a cubic grid with  $1 \text{ Mpc/h}$  spacing. The sum runs over all grid points within a distance of  $0.7 \cdot R_{\text{max}}$  from the void centre, where  $R_{\text{max}}$  is the radius of the largest selected void. The quantity  $\chi_i$  represents the  $i$ -th Cartesian component of the grid point in Lagrangian space with respect to the void center. The conservative choice of considering points within  $0.7 \cdot R_{\text{max}}$  was proposed by Sutter et al.

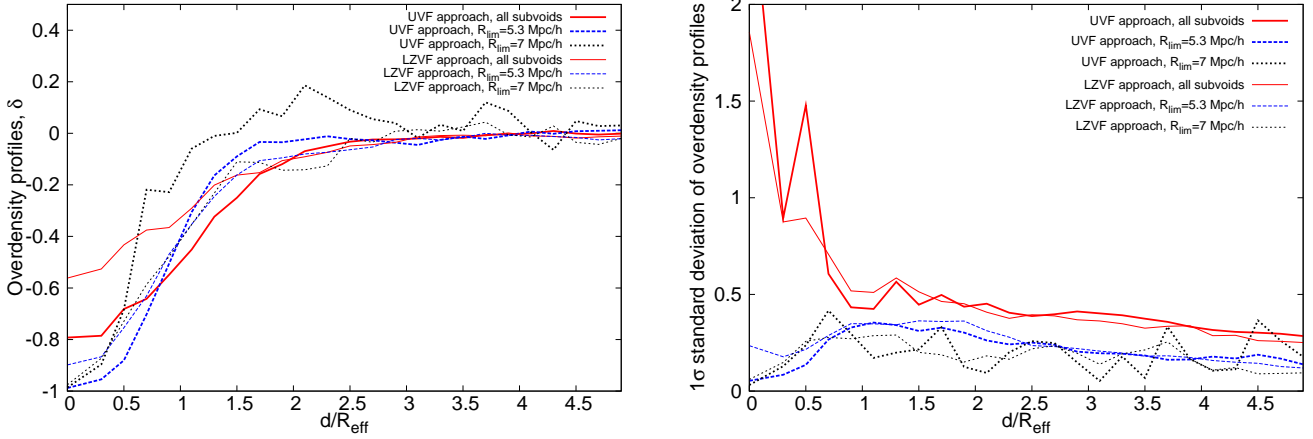


**Figure 6.** Mean overdensity profiles (*left-hand panel*) and corresponding  $1\sigma$  deviations (*right-hand panel*) of the voids detected by the two finders UVF and LZVF, as a function of the normalized radial distance,  $d/R_{\text{eff}}$ , and for three different values of  $R_{\text{lim}}$  (M centring), as indicated by the labels.

**Table 2.** Main parameters of the selected void samples. 1st and 2nd columns are the names of the void finders and the values of  $R_{\text{lim}}$ . 3rd and 4th columns show the average amplitudes of overdensity and divergence profiles in the central part of voids within  $0.2 \cdot R_{\text{eff}}$  with  $1\sigma$  standard deviation. The values in bracket show the ratio between the average values and their standard deviations (that is the significance of the signal). 5th and 6th columns show the radius range of the voids used for stacking and their numbers, respectively. 7th and 8th columns represent the average ellipticities  $\langle e \rangle$  of individual voids with  $1\sigma$  standard deviation, and the ellipticities of stacked voids  $e^{\text{st}}$ , respectively. Ellipticities are measured using the divergence field for UVF and LZVF voids, and using halo positions for ZOBOV voids.

void finder	$R_{\text{lim}}$	overdensity $\delta$	divergence $\Theta$	radius range, Mpc	N	$\langle e_{1,2} \rangle, \langle e_{1,3} \rangle$	$e_{1,2}^{\text{st}}$ and $e_{1,3}^{\text{st}}$
UVF	0	$-0.79 \pm 2.71$ (0.3)	$-1.53 \pm 0.80$ (1.9)	4-7	212	$0.82 \pm 0.11, 0.58 \pm 0.18$	$0.99 \pm 0.01, 0.97 \pm 0.01$
UVF	5.3	$-0.99 \pm 0.05$ (20)	$-2.47 \pm 0.57$ (4.3)	7-10	33	$0.79 \pm 0.12, 0.52 \pm 0.21$	$0.98 \pm 0.04, 0.97 \pm 0.05$
UVF	7	$-0.99 \pm 0.03$ (33)	$-2.57 \pm 0.48$ (5.4)	>7	7	$0.70 \pm 0.16, 0.47 \pm 0.09$	$0.63 \pm 0.24, 0.46 \pm 0.21$
LZVF	0	$-0.56 \pm 1.86$ (3.3)	$-1.68 \pm 0.87$ (1.7)	4-7	222	$0.84 \pm 0.11, 0.64 \pm 0.19$	$0.99 \pm 0.01, 0.98 \pm 0.01$
LZVF	5.3	$-0.90 \pm 0.23$ (3.9)	$-2.78 \pm 0.66$ (4.2)	7-10	50	$0.81 \pm 0.11, 0.61 \pm 0.17$	$0.97 \pm 0.03, 0.96 \pm 0.03$
LZVF	7	$-0.98 \pm 0.06$ (16.3)	$-3.29 \pm 0.61$ (5.4)	>7	15	$0.79 \pm 0.10, 0.47 \pm 0.18$	$0.89 \pm 0.09, 0.83 \pm 0.11$
ZOBOV		$-0.87 \pm 0.33$ (2.6)	$-0.37 \pm 1.00$ (0.4)	7-10	34	$0.76 \pm 0.10, 0.59 \pm 0.11$	$0.94 \pm 0.04, 0.89 \pm 0.04$

(2014) to balance between the need to consider a large number of grid points to maximise the signal-to-noise ratio and that of avoiding fluctuations that are effectively outside the void boundaries. We define the ellipticity,  $e$ , as the axial ratio of the eigenvalues  $\Lambda_i$  of the matrix  $I_{i,j}$  given by Eq. 9:

$$e_{1,2} = \sqrt{\Lambda_2/\Lambda_1}, \quad e_{1,3} = \sqrt{\Lambda_3/\Lambda_1}, \quad (7)$$

where  $\Lambda_1 \geq \Lambda_2 \geq \Lambda_3$ . The same definition has already been used by Plionis et al. (1991); de Theije et al. (1995); Splinter et al. (1997). The errors on the stacked void ellipticities are computed using the jackknife technique (Efron 1982). The average and stacked void ellipticities are reported in Table 2. The average ellipticity and its variance provide information on individual void shapes. Voids detected by our two finders have similar ellipticities, almost independent of  $R_{\text{lim}}$ . The ratio between major and medium axes is in the range  $0.70 - 0.84$  with  $\text{rms} \sim 0.1$ , and between major and minor axes in  $0.47 - 0.64$  with  $\text{rms} \sim 0.15$ . Voids look like elongated tri-axial ellipsoids. Overall, the void shape appears approximately similar, independently on which of our finders (UVF or LZVF) we use. Ellipticities of the stacked voids are close to unity, as expected, because our sample is not redshift-space distorted. Finally, we note that subvoids have on average a more spherical shape than larger voids.

## 5.5 Comparison with ZOBOV finder

We compare our results with those obtained with ZOBOV (Neyrinck 2008), a publicly available and widely used void finder algorithm that searches for depressions in the density distribution of a set of points. Applying a Voronoi tessellation, the algorithm associates a cell at each point, defined as the region that is closer to that point than to any other point of the sample. ZOBOV then identifies the local density minima, searching for the Voronoi-cells whose density is lower than that of all the other adjacent cells. The Voronoi-cells surrounding the local density minima are eventually joined, adding cells with larger and larger densities. Voids are identified as unions of these Voronoi-cells.

However, local density minima can be found also in overdense regions. To exclude the latter, we consider only regions with a overdensity minimum smaller than  $-0.8$  (Neyrinck 2008). To assess the statistical significance for each void, ZOBOV provides also the *fakeness probability*, that is the probability that a void is simply generated by Poisson fluctuations in the distribution of points. In this analysis, we consider only the voids with a significance level larger than  $2\sigma$ , as commonly assumed.

To assess ZOBOV void centres, we use the following definition:



$$\mathbf{x}_c = \frac{1}{V_{\text{void}}} \sum_{i=1}^{N_V} x_i^{\text{halo}} \cdot V_i^{\text{halo}}, \quad (8)$$

where  $\mathbf{x}_c$  is the baricentre,  $x_i$  and  $V_i^{\text{halo}}$  are the position of the  $i$ -th halo in the void and the volume of the associated Voronoi cell, respectively, and  $V_{\text{void}}$  is the volume provided by ZOBOV. The main properties of the ZOBOV void catalogue are reported in Tables 1 and 2. To compare our void finders with ZOBOV, we consider subsamples selected with  $R_{\text{lim}} = 5.3 \text{ Mpc}/h$ . This choice has no particular physical meaning. It just ensures that the number and effective radii of the voids selected with the three different finders are similar (see Table 1), and thus the statistical errors are similar as well. The interesting issue of how to determine the optimal value of  $R_{\text{lim}}$  for a specific cosmological analysis is postponed to a forthcoming paper.

The black line in Fig. 3 shows the cumulative distribution of the ZOBOV voids compared to our findings. While the total numbers of voids selected by UVF, LZVF and ZOBOV are similar, the ZOBOV voids appear systematically larger than the others. The median radii of UVF, LZVF (for  $R_{\text{lim}} = 5.3 \text{ Mpc}/h$ ) and ZOBOV are 7.0, 7.3 and 8.2  $\text{Mpc}/h$ , respectively. The filling factor of the ZOBOV voids is 56.4%, larger than the ones of our finders, 41% for UVF and 47% for LZVF.

A one-by-one comparison of the voids selected by the three finders is rather complicated, if not impossible, since different methods can select very different topological underdense structures. The two zoomed regions displayed in Fig. 7 show representative examples of two extreme cases. On the left-hand panel we zoom on a large void detected by all the three finders, approximately at the same positions. On the contrary, the region shown on the right-hand panel demonstrates that, in some cases, the underdense regions selected by ZOBOV can be entirely different than the ones detected by UVF and LZVF, while the latter are always in close agreement with each other. This is due to the significant differences in the methods. For example, the overdensity in the central part of the large void selected by UVF and LZVF (and not by ZOBOV) in the centre of the right-hand panel of Fig. 7 is  $-0.70 \pm 0.07$ , thus larger than the overdensity threshold used in ZOBOV.

Figs. 8 and 9 compare the mean divergence and overdensity profiles, and the corresponding  $1\sigma$  deviations, of the voids detected by the three finders UVF, LZVF and ZOBOV. As it can be seen, the UVF and LZVF profiles are steeper at small radial distances, and less scattered, especially the UVF one, consistent with the universality of the void shapes (Nadathur et al. 2014). The different profile shapes are caused by the very different approaches of the analysed Eulerian and Lagrangian void finders.

In Table 2 we compare the significance of the signal at the first radial bin, within  $0.2 \cdot R_{\text{eff}}$ , for both overdensity and divergence profiles. As it can be seen, the most prominent signal is in the overdensity profiles for ZOBOV, and in the divergence profiles for UVF and LZVF. However, the significance of the divergence signal obtained from both our finders is 60% higher than for overdensity profiles of ZOBOV voids. This may be explained by the fact that, for the calculation of the divergence field and corresponding void selection, we use randomised samples of haloes that are less biased by shot-noise in the central, extremely underdense, void regions.

For the ZOBOV voids we calculate the inertial tensor using the Eulerian coordinates of halos within  $0.7 \cdot R_{\text{max}}$  and assuming that all the haloes have equal masses,  $m = 1$ :

$$I_{i,j} = \sum_k \chi_{i,k} \chi_{j,k}, \quad (9)$$

where the index  $k$  corresponds to the index of the considered halo. UVF and LZVF have ellipticities closer to unity than ZOBOV ( $e_{1,2}^{\text{st}} = 0.98, 0.97$  and  $0.94$ , respectively), and the same  $\text{rms} \sim 0.04$ . For the ratio of major and minor axes, we also find systematically closer results to unity for UVF and LZVF than ZOBOV ( $0.97, 0.96$  and  $0.89$ , respectively).

## 6 SUMMARY AND CONCLUSIONS

Present and upcoming next generation galaxy redshift surveys, such as SDSS (Abazajian et al. 2009), BigBOSS (Schlegel et al. 2009), WFIRST (Green et al. 2012), HETDEX (Hill et al. 2008), and Euclid (Laureijs et al. 2011), will provide spectroscopic data with unprecedented large statistics, allowing the use of underdense regions as effective cosmological probes. One of the most promising applications for cosmology is to exploit void ellipticities (Lavaux & Wandelt 2010; Sutter et al. 2012).

The identification of cosmic voids, however, is not trivial, due to their large sizes and peculiar structures. Generally, void finders are based on density or geometric criteria, which can be affected by large shot noise. In this work we implemented two dynamical void finders, not affected by this weakness, and characterised by a minimal number of free parameters and additional assumptions. The proposed void finders are based on sample randomisation. One uses the Zel'dovich approximation to trace back in time the orbits of matter tracers. The second uses the observed two-point correlation function to relax the objects' spatial distribution to homogeneity. The Lagrangian Zel'dovich Void Finder is similar to the DIVA procedure for what concerns the displacement field reconstruction (Lavaux & Wandelt 2010). On the other hand, the Uncorrelating Void Finder adopts a new technique based on the measurement of the two-point correlation function of the sample. The two independent dynamical void finders considered in this work are thus complementary, and allowed us to strengthen our main results and conclusions.

We defined voids as sinks of the back-in-time streamlines of the mass tracers in Lagrangian coordinates using the divergence of the displacement field. With a watershed technique (Platen et al. 2007) we identified hundreds of subvoids around the local minima of the divergence field. These subvoids are parents of larger voids, which we constructed using criteria of minimal effective void radius. Moreover, we considered four different approaches for the definition of void centres, a crucial issue for a proper void stacking. We found that the most convenient option is the stacking of voids centred on their minimum divergence. To test our finders we used a halo catalogue from the CoDECS simulations.

We compared our results with those obtained with the publicly available Eulerian class ZOBOV finder, using the same halo catalogue at  $z = 0$ . We found that the overdensity profiles of both UVF and LZVF are more self-similar than the ZOBOV ones, thus their stacking should provide more accurate cosmological probes. The significance of the signal in the central part of the voids ( $< 0.2 R_{\text{eff}}$ ) is 60% higher for the divergence profiles of our voids than for overdensity profiles of ZOBOV voids, when using Eulerian halo positions. We measured the ellipticities of both individual voids and stacked ones. We found a good agreement between individual void shapes for all the three finders with average axis ratios  $< e_{1,2} > \sim 0.8 \pm 0.1$ ,  $< e_{1,3} > \sim 0.55 \pm 0.15$ . The void shape appears approximately universal, independent of the fact that voids are detected using overdensities or divergences. Stacked voids from both our finders have much more spherical shape than ZOBOV ones. The

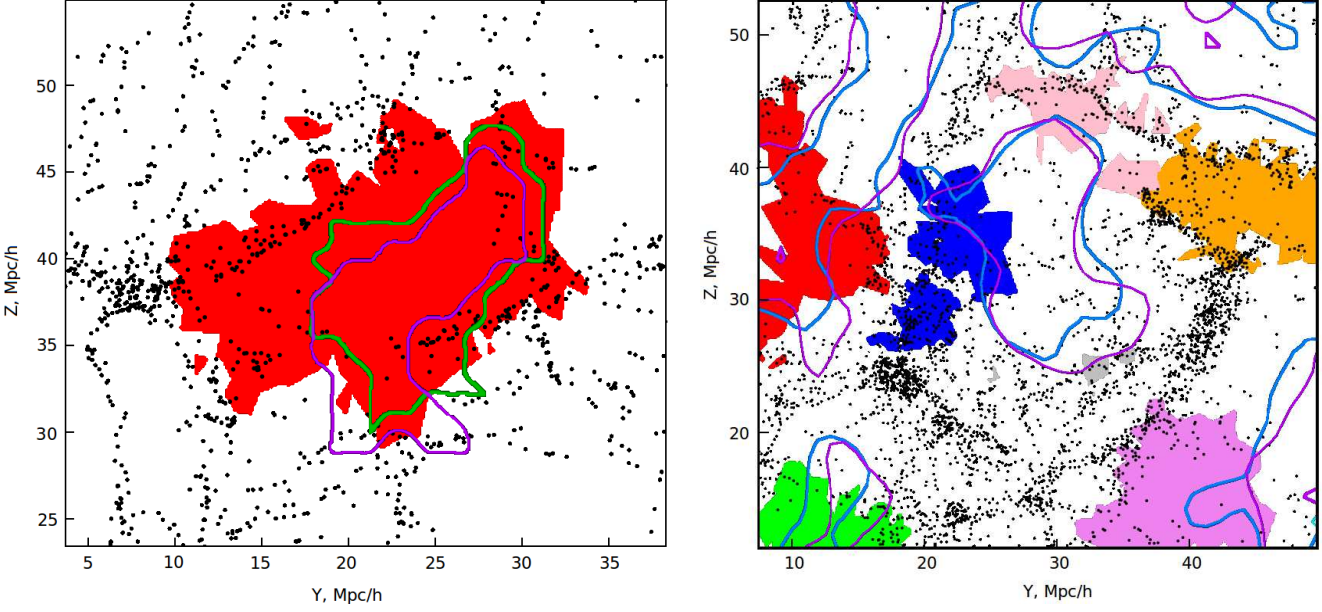


**Figure 7.** Zoom of two regions of the slice shown in Fig. 1. Thick and thin lines show the shapes of voids selected by UVF and LZVF finders, respectively. Filled coloured areas show the voids found by ZOBOV. The underdense regions selected by UVF and LZVF appear always similar. On the other hand, voids selected by ZOBOV are in some cases similar to the ones detected by the other two finders (*left-hand panel*), while in other cases are very different (*right-hand panel*).

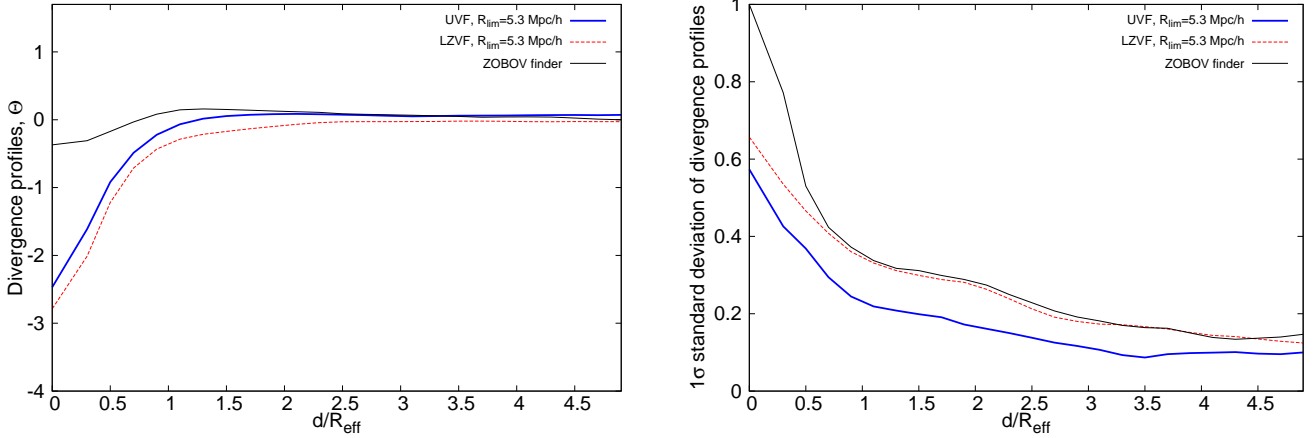


**Figure 8.** Comparison between the mean divergence profiles (*left-hand panel*) and corresponding  $1\sigma$  deviations (*right-hand panel*) of the voids detected by the two finders UVF and LZVF and the ones detected by ZOBOV, as a function of the normalized radial distance,  $d/R_{\text{eff}}$ .

voids' properties of both our finders are in good agreement with each other. The two proposed void finders can thus complement the existing set of finders and contribute to improve the accuracy of cosmological probes.

The forthcoming Euclid survey will be very promising for the application of our dynamical void finders. The expected spectroscopic survey will cover 15000 sq. deg. and will contain around  $5 \cdot 10^7$  galactic redshifts, mainly in the range  $0.7 < z < 2.1$ , up to visual magnitude  $m_H = 24$  (Laureijs et al. 2011). At such redshift range the mean spacing will rise just from 4 to 15 Mpc/h (Biswas et al. 2010). This makes the Euclid spectroscopic survey an ideal laboratory for the studying of voids' evolution. The volume of the Euclid spectroscopic survey will be larger than that of SDSS by a factor of 500. So we expect 300 times more galaxies and few hundreds times more voids in comparison to SDSS.

In the work by Biswas et al. (2010) it has been shown that such a high statistics of void ellipticities, combined with other traditional methods, is expected to improve the DE task force figure of merit (FoM) on the DE parameters by orders of hundreds. The simulation of Lavaux & Wandelt (2012) showed the effectiveness of the Euclid stacked voids for the AP test and further DE probes. The FoM of stacked voids from the Euclid survey may double all the other DE probes derived from the Euclid data alone (combined with Planck priors). Moreover, the Euclid voids could in principle improve the outcomes from baryon acoustic oscillations by an order of magnitude. The cosmological constraints that can be obtained with the CMB gravitational lensing on cosmic voids for a Euclid-like survey have been investigated by Chantavat et al. (2014). The authors found that the latter could be comparable to the constraints from Planck data alone.

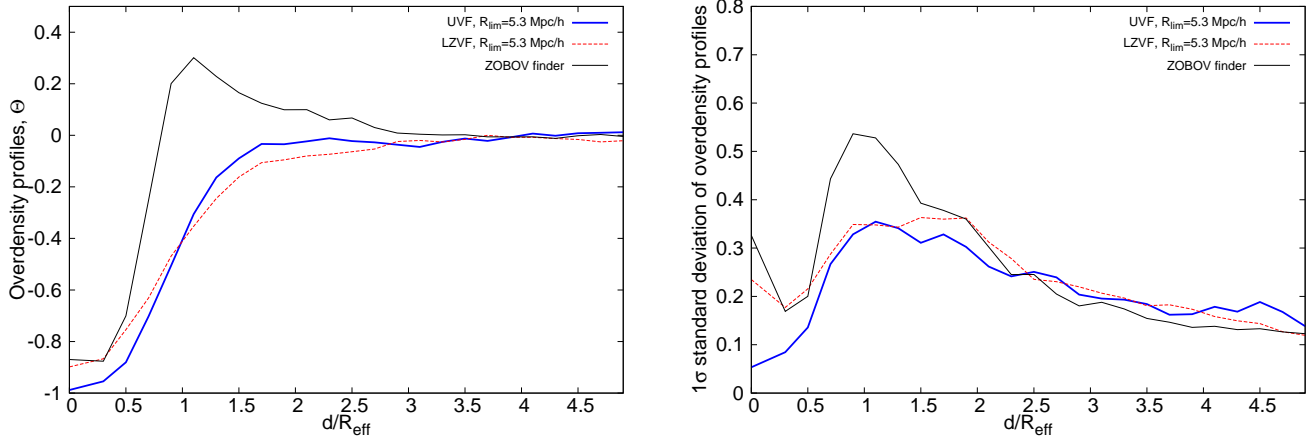


**Figure 9.** Comparison between the mean overdensity profiles (*left-hand panel*) and corresponding  $1\sigma$  deviations (*right-hand panel*) of the voids detected by the two finders UVF and LZVF and the ones detected by ZOBOV, as a function of the normalized radial distance,  $d/R_{\text{eff}}$ .

In a forthcoming paper we plan to further investigate the characteristics of the cosmic voids detected by the proposed finders, in particular the redshift evolution of the void number density, size distribution and ellipticities, and their dependence on the cosmological model. We will also investigate the effect of redshift-space distortions in the divergence field.

## ACKNOWLEDGMENTS

We acknowledge the grants ASI n.I/023/12/0 "Attività relative alla fase B2/C per la missione Euclid" and MIUR PRIN 2010-2011 "The dark Universe and the cosmic evolution of baryons: from current surveys to Euclid". MB is supported by the Marie Curie Intra European Fellowship "SIDUN" within the 7th Framework Programme of the European Commission. The numerical simulations presented in this work have been performed and analysed on the Hydra cluster at the RZG supercomputing centre in Garching, and on the BladeRunner cluster at the Bologna University, partly funded by the Marie Curie Intra European Fellowship "SIDUN". We acknowledge financial support from PRIN INAF 2012 The Universe in the box: multiscale simulations of cosmic structure.

## REFERENCES

- Abazajian, K. N., Adelman-McCarthy, J. K., Agüeros, M. A., et al. 2009, *ApJS*, 182, 543
- Ahn, C. P., Alexandroff, R., Allende Prieto, C., et al. 2014, *ApJ Suppl.*, 211, 17
- Alcock, C., & Paczynski, B. 1979, *Nature*, 281, 358
- Amendola, L. 2000, *PhRvD*, 62, 043511
- Amendola, L., Appleby, S., Bacon, D., et al. 2013, *Living Reviews in Relativity*, 16, 6
- Aragon-Calvo, M. A., & Szalay, A. S. 2013, *MNRAS*, 428, 3409
- Arlen, T. C., & Vassiliev, V. V. 2013, *arXiv:1303.2121*
- Bahcall, N. A. 1995, *PASP*, 107, 790
- Baldi, M. 2012, *MNRAS*, 422, 1028
- Baldi, M., Pettorino, V., Robbers, G., & Springel, V. 2010, *MNRAS*, 403, 1684
- Bardeen, J. M., Bond, J. R., Kaiser, N., & Szalay, A. S. 1986, *ApJ*, 304, 15
- Beck, A. M., Hanasz, M., Lesch, H., Remus, R.-S., & Stasyszyn, F. A. 2013, *MNRAS*, 429, L60
- Biswas, R., Alizadeh, E., & Wandelt, B. D. 2010, *PhRD*, 82, 023002
- Bos, E. G. P., van de Weygaert, R., Dolag, K., & Pettorino, V. 2012, *MNRAS*, 426, 440
- Brenier, Y., Frisch, U., Hénon, M., et al. 2003, *MNRAS*, 346, 501
- Brunino, R., Trujillo, I., Pearce, F. R., & Thomas, P. A. 2007, *MNRAS*, 375, 184
- Cai, Y.-C., Padilla, N., & Li, B. 2014, *arXiv:1410.1510*
- Chantavat, T., Sawangwit, U., Sutter, P. M., & Wandelt, B. D. 2014, *arXiv:1409.3364*
- Clampitt, J., & Jain, B. 2014, *arXiv:1404.1834*
- Clampitt, J., Cai, Y.-C., & Li, B. 2013, *MNRAS*, 431, 749
- Colberg, J. M., Sheth, R. K., Diaferio, A., Gao, L., & Yoshida, N. 2005, *MNRAS*, 360, 216
- Colberg, J. M., Pearce, F., Foster, C., et al. 2008, *MNRAS*, 387, 933
- Courtois, H. M., Hoffman, Y., Tully, R. B., & Gottlöber, S. 2012, *ApJ*, 744, 43
- Croft, R. A. C., & Gaztanaga, E. 1997, *MNRAS*, 285, 793
- D'Amico, G., Musso, M., Noreña, J., & Paranjape, A. 2011, *Phys.Rev.D*, 83, 023521
- Davis, M., Efstathiou, G., Frenk, C. S., & White, S. D. M. 1985, *ApJ*, 292, 371
- de Theije, P. A. M., Katgert, P., & van Kampen, E. 1995, *MNRAS*, 273, 30
- DeLavallaz, A., & Fairbairn, M. 2012, *Physical Review Letters*, 108, 171301
- Efron, B. "The jackknife, the bootstrap, and other resampling plans". Society of Industrial and Applied Mathematics CBMS-NSF Monographs, 38.
- Elyiv, A., Neronov, A., & Semikoz, D. V. 2009, *PhRvD*, 80, 023010
- Elyiv, A. A., Karachentsev, I. D., Karachentseva, V. E., Melnyk, O. V., & Makarov, D. I. 2013, *Astrophysical Bulletin*, 68, 1
- Geller, M. J., & Huchra, J. P. 1989, *Science*, 246, 897
- Gibbons, G. W., Werner, M. C., Yoshida, N., & Chon, S. 2014, *MNRAS*, 438, 1603
- Gottlöber, S., Łokas, E. L., Klypin, A., & Hoffman, Y. 2003, *MNRAS*, 344, 715
- Green, J., Schechter, P., Baltay, C., et al. 2012, *arXiv:1208.4012*

- Gregory S. A. & Thompson L. A. 1978, *ApJ*, 222, 784
- Hahn O., Porciani C., Carollo C. M., Dekel A., 2007, *MNRAS*, 375, 489
- Hellwing, W. A., Juszkievicz, R., & van de Weygaert, R. 2010, *PhRvD*, 82, 103536
- Hill, G. J., Gebhardt, K., Komatsu, E., et al. 2008, *Panoramic Views of Galaxy Formation and Evolution*, 399, 115
- Huchra, J. P., Geller, M. J., de Lapparent, V., & Burg, R. 1988, *Large Scale Structures of the Universe*, 130, 105
- Izumi, K., Hagiwara, C., Nakajima, K., Kitamura, T., & Asada, H. 2013, *Phys.Rev.D*, 88, 024049
- Joeveer, M., Einasto, J., & Tago, E. 1978, *MNRAS*, 185, 357
- Kaiser, N., Aussel, H., Burke, B. E., et al. 2002, *Proceedings of the SPIE*, 4836, 154
- Karachentsev, I. D., Makarov, D. I., Karachentseva, V. E., & Melnyk, O. V. 2011, *Astrophysical Bulletin*, 66, 1
- Kovács, A., Szapudi, I., Granett, B. R., et al. 2014, *arXiv:1407.1470*
- Krakau, S., & Schlickeiser, R. 2014, *ApJ*, 789, 84
- Krause, E., Chang, T.-C., Doré, O., & Umetsu, K. 2013, *ApJ*, 762, L20
- Kreckel, K., Peebles, P. J. E., van Gorkom, J. H., van de Weygaert, R., & van der Hulst, J. M. 2011, *AJ*, 141, 204
- Laureijs, R., Amiaux, J., Arduini, S., et al. 2011, *arXiv:1110.3193*
- Lavaux, G., & Wandelt, B. D. 2010, *MNRAS*, 403, 1392
- Lavaux, G., & Wandelt, B. D. 2012, *ApJ*, 754, 109
- Leclercq, F., Jasche, J., Sutter, P. M., Hamaus, N., & Wandelt, B. 2014, *arXiv:1410.0355*
- Li B., 2011, *MNRAS*, 411, 2615
- Lindner, U., Einasto, J., Einasto, M., et al. 1995, *A&A*, 301, 329
- Marulli, F., Bianchi, D., Branchini, E., et al. 2012, *MNRAS*, 426, 2566
- Marulli, F., Bolzonella, M., Branchini, E., et al. 2013, *A&A*, 557, A17
- Melchior, P., Sutter, P. M., Sheldon, E. S., Krause, E., & Wandelt, B. D. 2014, *MNRAS*, 440, 2922
- Miniati, F., & Elyiv, A. 2013, *ApJ*, 770, 54
- Montero-Dorta, A. D., & Prada, F. 2009, *MNRAS*, 399, 1106
- Nadathur, S., Hotchkiss, S., Diego, J. M., et al. 2014, *arXiv:1407.1295*
- Neyrinck, M. C. 2008, *MNRAS*, 386, 2101
- Nicholls, D. C., Jerjen, H., Dopita, M. A., & Basurah, H. 2014, *ApJ*, 780, 88
- Nusser, A., & Branchini, E. 2000, *MNRAS*, 313, 587
- Odrzywołek, A. 2009, *PhRvD*, 80, 103515
- Patiri, S. G., Betancort-Rijo, J. E., Prada, F., Klypin, A., & Gottlöber, S. 2006, *MNRAS*, 369, 335
- Peebles, P. J. E. 1980, *Research supported by the National Science Foundation*. Princeton, N.J., Princeton University Press, 1980. 435 p.,
- Peebles, P. J. E. 2001, *ApJ*, 557, 495
- Peebles, P. J. E. 1989, *ApJ*, 344, L53
- Platen, E., van de Weygaert, R., & Jones, B. J. T. 2007, *MNRAS*, 380, 551
- Plionis, M., & Basilakos, S. 2002, *MNRAS*, 330, 399
- Plionis, M., Barrow, J. D., & Frenk, C. S. 1991, *MNRAS*, 249, 662
- Pollina et al. 2014, in preparation
- Rees, M. J., & Sciama, D. W. 1968, *Nature*, 217, 511
- Ricciardelli, E., Quilis, V., & Planelles, S. 2013, *MNRAS*, 434, 1192
- Rintoul, M. D., & Torquato, S. 1997, *J. Colloid Interface Sci.*, 186, 467
- Sahni, V., & Shandarin, S. 1996, *MNRAS*, 282, 641
- Schlegel, D. J., Bebek, C., Heetderks, H., et al. 2009, *arXiv:0904.0468*
- Schlickeiser, R., Elyiv, A., Ibscher, D., & Miniati, F. 2012, *ApJ*, 758, 101
- Shandarin, S., Feldman, H. A., Heitmann, K., & Habib, S. 2006, *MNRAS*, 367, 1629
- Sheth, R. K., & van de Weygaert, R. 2004, *MNRAS*, 350, 517
- Soares-Santos, M., de Carvalho, R. R., Annis, J., et al. 2011, *ApJ*, 727, 45
- Splinter, R. J., Melott, A. L., Linn, A. M., Buck, C., & Tinker, J. 1997, *ApJ*, 479, 632
- Spolyar, D., Sahlén, M., & Silk, J. 2013, *Physical Review Letters*, 111, 241103
- Springel, V., White, S. D. M., Tormen, G., & Kauffmann, G. 2001, *MNRAS*, 328, 726
- Stanonik, K., Platen, E., Aragón-Calvo, M. A., et al. 2010, *Galaxies in Isolation: Exploring Nature Versus Nurture*, 421, 107
- Sutter, P. M., Lavaux, G., Wandelt, B. D., & Weinberg, D. H. 2012, *ApJ*, 761, 187
- Sutter, P. M., Pisani, A., & Wandelt, B. D. 2014, *arXiv:1404.5618*
- Sutter, P. M., Lavaux, G., Wandelt, B. D., Weinberg, D. H., & Warren, M. S. 2014, *MNRAS*, 438, 3177
- Szapudi, I., Kovács, A., Granett, B. R., et al. 2014, *arXiv:1406.3*
- Tikhonov, A. V., & Karachentsev, I. D. 2006, *ApJ*, 653, 969
- Tully, R. B., Courtois, H. M., Dolphin, A. E., et al. 2013, *ApJ*, 766, 86
- Vavilova, I. B., Melnyk, O. V., & Elyiv, A. A. 2009, *Astronomische Nachrichten*, 330, 1004
- Wetterich, C. 1995, *A&A*, 301, 321
- Zel'dovich, Y. B. 1970, *A&A*, 5, 84
- Zivick, P. M., Sutter S. 2014, *arXiv:1410.0133*

